


## Roles of electrons on the thermal transport of 2D metallic MXenes

Ao Wang, Shouhang Li, Xinyu Zhang, and Hua Bao <sup>\*</sup>

*University of Michigan-Shanghai Jiao Tong University Joint Institute, Shanghai Jiao Tong University, Shanghai 200240, People's Republic of China*

 (Received 8 October 2021; revised 12 December 2021; accepted 5 January 2022; published 26 January 2022)

MXenes have many potential applications in electronics, energy storage, sensors, thermal management, and biomedical catalysis. As one of the most widely explored two-dimensional (2D) materials, their transport properties are of broad interest. Due to the difficulty in direct experimental measurements of their thermal conductivity, existing works mainly rely on theoretical approaches. However, only lattice contribution to thermal conductivity in MXenes was studied in previous works, while the role of electrons in thermal transport MXenes has never been elucidated. Herein, we investigate the electron and phonon contribution to the thermal conductivity of three typical metallic 2D MXenes [ $\text{Ti}_2\text{CF}_2$ ,  $\text{Ti}_2\text{CCl}_2$ , and  $\text{Ti}_2\text{C}(\text{OH})_2$ ] with a first-principles approach, in which the mode-level electron-phonon coupling is rigorously considered. The thermal conductivity values are predicted to be 69.1, 104.7, and 54.3 W/mK for  $\text{Ti}_2\text{CF}_2$ ,  $\text{Ti}_2\text{CCl}_2$ , and  $\text{Ti}_2\text{C}(\text{OH})_2$ , respectively. The contribution of electron to total thermal conductivity (37.3–61.3%) is much larger than most existing 2D materials. We find that the relatively large electron density in metallic MXenes leads to the considerable electronic thermal conductivity. Moreover, due to large phonon-electron scattering phase space and matrix element, the phonon thermal conductivity is largely suppressed by the scattering with electrons. Our results clarify the role of electrons in the thermal transport in metallic MXenes and can provide a deeper understanding of the transport mechanism in metallic 2D materials.

DOI: [10.1103/PhysRevMaterials.6.014009](https://doi.org/10.1103/PhysRevMaterials.6.014009)

### I. INTRODUCTION

Two-dimensional (2D) materials, such as graphene,  $\text{MoS}_2$ , and phosphorene, possess exceptional mechanical, electrical, and thermal properties, which have aroused tremendous research interest in the past decade. MXene is a family of 2D transition-metal carbides, nitrides, or carbonitrides, and was first synthesized in 2011 [1]. Specifically, metallic MXenes are believed to have outstanding electrical conductivity [2,3], flexibility [3], and tunable work function [4]. Therefore, they are expected to have wide applications in flexible triboelectric nanogenerators [2], Li-ion storage materials [3,5], ion batteries [6], gas sensors [7], and solar cells [4,8].

Recently, there has also been growing interest to use metallic MXenes as a filler to enhance the thermal conductivity of composite materials. For example, metallic  $\text{Ti}_3\text{C}_2$  MXene was shown to enhance the thermal conductivity of styrene-butadiene rubber system by  $1.5\times$  with only 2% by weight, holding great superiority compared to reduced graphene oxide [9]. Also, the thermal conductivity of nitrile butadiene rubber is found to increase by  $1.88\times$  with a 20% volume fraction of metallic  $\text{Ti}_3\text{C}_2T_x$  MXene filler [10]. All these studies implied that MXenes should have high thermal conductivity. Nevertheless, there are no direct measured intrinsic thermal conductivities of pristine MXenes, likely due to the challenges in experiments [11]. This has become the primary obstacle to understand and further improve the heat dissipation ability of MXene-based composite materials. On the other hand, thermal transport in 2D materials generally show quite distinct

behaviors. For graphene, the thermal conductivity reaches  $\sim 2700$  W/mK [12] due to the decoupling of in-plane and out-of-plane lattice vibrations [13]. In comparison, 2D tellurium has thermal conductivity as low as 2.16 W/mK owing to its strong lattice anharmonicity [14]. These observations are all attributed to the diverse and complicated phonon transport mechanism. In comparison to phonons, electrons can also be important heat carriers in metallic MXenes. As far as we know, the electron thermal transport mechanism for 2D metallic materials has never been explored. Therefore, in order to obtain the thermal conductivity of MXenes and further understand the thermal transport mechanism in 2D metallic materials, a thorough investigation of the thermal transport of metallic MXenes is highly desirable.

In this work, we choose three metallic MXenes with different functional groups, including  $\text{Ti}_2\text{CF}_2$ ,  $\text{Ti}_2\text{CCl}_2$ , and  $\text{Ti}_2\text{C}(\text{OH})_2$  as prototypes. Our investigations are carried out using the state-of-the-art computational scheme with rigorous consideration of the electron-phonon interactions [15–22]. The electron and phonon contributions to the thermal transport are elucidated. Different from the previous cognition [23] that phonons are the main heat carriers, the electrons are found to contribute a significant amount of thermal transport, while they reduce the phonon thermal conductivity by relatively strong scattering with phonons. The thermal transport mechanisms in metallic MXenes are also compared with other 2D materials and discussed.

### II. METHODS

The electron and phonon thermal conductivity are calculated based on the relaxation time

<sup>\*</sup>hua.bao@sjtu.edu.cn

approximation of Boltzmann-transport equation [24], with the expression of

$$\kappa_{\alpha\beta}^{el(ph)} = \frac{1}{N_{\lambda}} \sum_{\lambda} c_{\lambda}^{el(ph)} v_{\lambda,\alpha}^{el(ph)} v_{\lambda,\beta}^{el(ph)} \tau_{\lambda}^{el(ph)}. \quad (1)$$

$c$ ,  $v$ , and  $\tau$  are the heat capacity, group velocity, and relaxation time, respectively.  $\lambda$  denotes the modes of electron and phonon, with total of  $N$  points in the Brillouin zone.  $\alpha$  and  $\beta$  denote the Cartesian directions. The modal heat capacity and group velocity can be determined from the electronic band structure and phonon dispersion. The detailed expressions for electron and phonon relaxation times can be found in the Supplemental Material [25].

To get the electronic transport properties, the Electron-Phonon Wannier (EPW) package [26] is employed to determine the mode-level electron relaxation times limited by electron-phonon scatterings. The coarse  $\mathbf{k}/\mathbf{q}$ -points meshes are interpolated into a dense mesh of  $100 \times 100 \times 1$  to obtain the converged electrical transport properties using the Wannier interpolation technique [27]. We then employ the electron Boltzmann transport equation (BTE), with all the inputs (electron energy, group velocity, and relaxation time) from the first-principles calculations to obtain the electronic thermal conductivity and electrical conductivity. Note that the direct output electron lifetimes of the EPW package are not used in our work. Based on the latest understanding [18], energy relaxation times should be employed for electronic thermal conductivity while momentum relaxation times should be used for electrical conductivity. Therefore, the EPW package is modified based on electron relaxation time expressions in Sec. S1 in the Supplemental Material [25]. To show that electron-electron scattering can be neglected, we also calculate electron-electron scattering rates with the *GW* approximation [28]. We implement the single-shot *GW* ( $G_0W_0$ ) in the YAMBO package [29] and use  $30 \times 30 \times 1$   $\mathbf{k}$ -points mesh and 100 empty electron bands in the calculations.

We calculate the phonon transport properties with the anharmonic lattice dynamics approach [30–32]. We use a  $5 \times 5 \times 1$  supercell with a cutoff of the sixth-nearest atom to calculate the cubic force constants using the finite-difference method [33]. Then, we employed the SHENGBTE package [33] to calculate the phonon thermal conductivity with iterative method. The  $\mathbf{q}$ -points mesh is set to be  $100 \times 100 \times 1$ . The phonon-electron scattering is further considered to obtain the effective phonon scattering rates using Matthiessen's rule [34] ( $1/\tau_{\lambda} = 1/\tau_{\lambda}^{pp} + 1/\tau_{\lambda}^{pe}$ , where  $\lambda$  denotes the phonon modes;  $1/\tau_{\lambda}^{pp}$  and  $1/\tau_{\lambda}^{pe}$  are the phonon-phonon and phonon-electron scattering rates, respectively).

We carry out the first-principles simulation with the QUANTUM ESPRESSO package [35]. To model 2D MXenes, a vacuum layer of more than 10 Å is introduced in the simulation domain to eliminate the interactions between different layers. The Perdew-Burke-Ernzerhof form of exchange-correlation functional pseudopotential [36] is employed. The cutoff energy of plane waves is set as 80 Ry. An  $8 \times 8 \times 1$  Monkhorst-Pack  $\mathbf{k}$ -points mesh is used for the self-consistent calculation for  $\text{Ti}_2\text{CF}_2$  and  $\text{Ti}_2\text{C}(\text{OH})_2$ . The mesh for  $\text{Ti}_2\text{CCl}_2$  is set to be  $10 \times 10 \times 1$  to ensure the convergence. The convergence threshold of electron energy is set to be  $10^{-10}$  Ry. The

Broyden-Fletcher-Goldfarb-Shanno method [37–40] is used to optimize the structure. The  $10 \times 10 \times 1$  mesh is set to  $\mathbf{q}$  points in the density-functional perturbation theory [41] calculations to obtain the harmonic force constants and phonon perturbations.

### III. RESULTS AND DISCUSSION

#### A. Crystal structures, electronic band structures, and phonon dispersions

We construct initial atomic structures of the three metallic MXenes based on previous studies [42,43]. The crystal structures with the stable hexagonal phase are shown in Fig. 1(a). MXenes studied here have monolayer  $T$ -Ti-C-Ti- $T$  ( $T = \text{F}, \text{Cl}, \text{OH}$ ) along the  $c$  axis. The optimized lattice parameters on the  $a$  axis for  $\text{Ti}_2\text{CF}_2$ ,  $\text{Ti}_2\text{CCl}_2$ , and  $\text{Ti}_2\text{C}(\text{OH})_2$  are 3.06, 3.24, and 3.07 Å, respectively, which are consistent with previous first-principles simulations [23,43]. The optimized thicknesses ( $d$ ) for  $\text{Ti}_2\text{CF}_2$ ,  $\text{Ti}_2\text{CCl}_2$ , and  $\text{Ti}_2\text{C}(\text{OH})_2$  are 4.78, 5.54, and 6.78 Å, respectively. Note that the definition of thickness of 2D materials can be arbitrary [44–46]. Different definitions of thickness can affect the effective volume, resulting in deviations in the calculated thermal conductivity of 2D materials. Here we define the thickness in MXenes to be the distance between  $T$  atoms (for OH, the hydrogen atoms) on the  $c$  axis to keep consistent with the previous definition [46–48]. Note that we only consider the thermal conductivity  $\kappa$  of monolayer MXenes. If the interlayer coupling effect can be neglected, the thermal conductivity of multilayer MXenes can be estimated by  $\kappa \cdot (d/d_{\text{eff}})$ , where  $d_{\text{eff}}$  is the effective layer thickness in real multilayer samples.

The calculated electronic band structure of  $\text{Ti}_2\text{C}(\text{OH})_2$  is shown in Fig. 1(b). The band structures for the other two MXenes are similar (see Fig. S1), and are not shown here for clarity. All three MXenes are metallic since the Fermi level intersects with the electronic bands. The phonon spectrum for  $\text{Ti}_2\text{C}(\text{OH})_2$  is shown in Fig. 1(c). No imaginary frequencies are observed, indicating that the structure is stable. Quadratic flexural acoustic (ZA) phonon mode near the  $\Gamma$  point is observed, which is a typical characteristic of 2D materials compared to 3D materials [49,50]. The high optical phonon frequencies ( $> 100$  THz) for  $\text{Ti}_2\text{C}(\text{OH})_2$  are due to the light atomic mass of hydrogen atoms. The dispersions of  $\text{Ti}_2\text{CF}_2$  and  $\text{Ti}_2\text{CCl}_2$  show similar characteristics and are shown in Fig. S2. The electronic band structures and phonon spectra are consistent with the previous first-principles work [48].

#### B. Total thermal conductivity

The total thermal conductivities of the MXenes are shown in Figs. 2(a)–2(c). The values are, respectively, 69.1, 104.7, and 54.3 W/mK for  $\text{Ti}_2\text{CF}_2$ ,  $\text{Ti}_2\text{CCl}_2$ , and  $\text{Ti}_2\text{C}(\text{OH})_2$  at 300 K. Overall, the total thermal conductivities for metallic MXenes are larger than the theoretical values of nonmetallic MXenes including  $\text{Ti}_2\text{CO}_2$  (23 W/mK) and  $\text{Zr}_2\text{CO}_2$  (61 W/mK) [46]. Since there are no direct experimental results to compare with, we compare our predicted value with the experimental data for MXene thin film ( $\text{Ti}_3\text{C}_2\text{T}_z$ ) with a mixture of  $-\text{O}$ ,  $-\text{F}$ , and  $-\text{OH}$  functional groups [51]. Our calculated values for  $\text{Ti}_2\text{CF}_2$  and  $\text{Ti}_2\text{C}(\text{OH})_2$  are

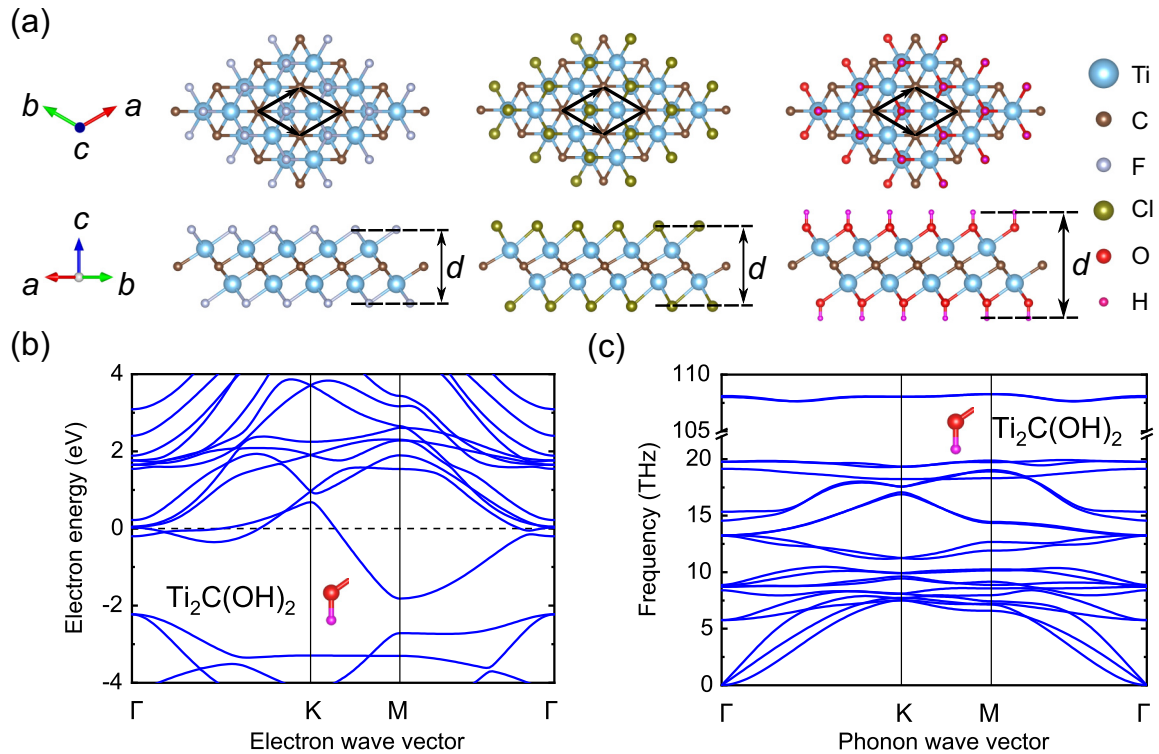


FIG. 1. (a) Top and side views of the crystal structure of the three metallic MXenes. The black boxes indicate the corresponding unit cells. The thicknesses of monolayer MXenes are denoted by dashed lines in the second row. (b) The calculated electronic band structure and (c) phonon dispersion of  $\text{Ti}_2\text{C}(\text{OH})_2$ .

comparable to the experimental thermal conductivity of  $\text{Ti}_3\text{C}_2\text{T}_z$  (55.8 W/mK) [51]. MXenes are often employed as fillers to enhance the thermal conductivity of composite materials. However, the thermal conductivity of metallic MXenes shown here are found to be much smaller than that of graphene.

### C. Electrical transport properties

To obtain a deeper understanding of the thermal transport mechanisms in metallic MXenes, we further examine the separated electron and phonon contributions to thermal conductivity, as shown in Fig. 2. The electronic thermal con-

ductivity values at 300 K are 42.4, 39.1, and 24.4 W/mK for  $\text{Ti}_2\text{CF}_2$ ,  $\text{Ti}_2\text{CCl}_2$ , and  $\text{Ti}_2\text{C}(\text{OH})_2$ , respectively. The electronic thermal conductivities of the three MXenes are almost temperature independent, resulting from the competition between the decrease of electron relaxation time and the increase of electron heat capacity with temperature [52]. There is still a slight increase in the electronic thermal conductivity when the temperature is higher than 400 K. This phenomenon is caused by the increase of average electron group velocity at higher temperatures (see Fig. S3). The contribution of electrons to the thermal conductivity is relatively large (37.3–61.3% at 300 K). This considerable contribution is mainly induced by the

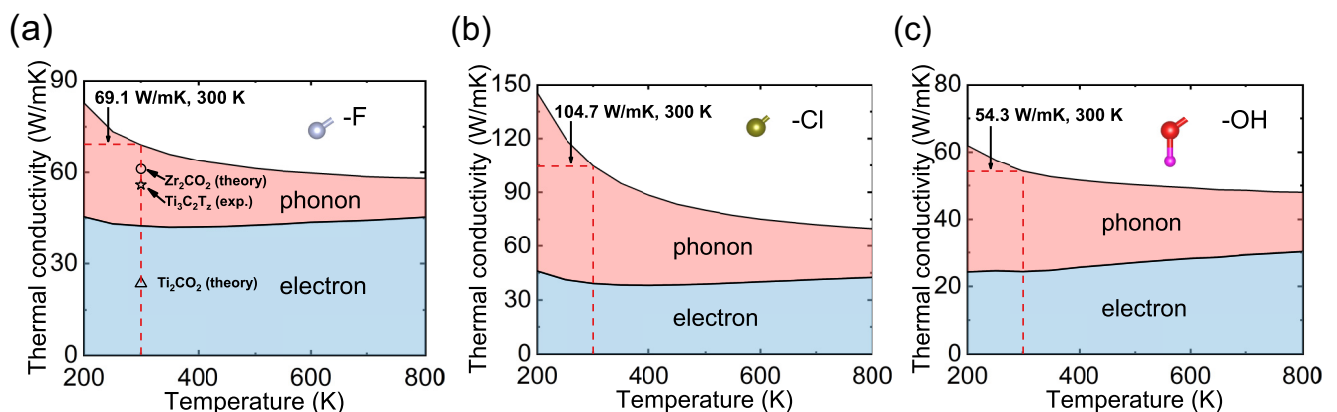


FIG. 2. Electron thermal conductivity and phonon thermal conductivity from 200 to 800 K for (a)  $\text{Ti}_2\text{CF}_2$ , (b)  $\text{Ti}_2\text{CCl}_2$ , and (c)  $\text{Ti}_2\text{C}(\text{OH})_2$ . The hollow scatters in (a) are the data for some other typical MXenes from first-principles calculation [46] (theory) and experiment [51] (exp.).

TABLE I. The electron properties of the MXenes and Cu at 300 K.

Material	Ti <sub>2</sub> CF <sub>2</sub>	Ti <sub>2</sub> CCl <sub>2</sub>	Ti <sub>2</sub> C(OH) <sub>2</sub>	Cu
Electronic volumetric specific heat ( $10^4$ J/m <sup>3</sup> K)	5.52	3.77	4.60	3.10
Average electron group velocity ( $10^5$ m/s)	2.89	2.27	2.10	6.52
Average electron relaxation time (fs)	8.14	16.4	8.42	27.7
Mean-free path (nm)	2.4	3.7	1.8	18.1

large electron carrier concentration, which is in the range of  $2.6\text{--}5.8 \times 10^{22} \text{ cm}^{-3}$  in metallic MXenes from first-principles calculations [see Eq. (S13)].

To understand the differences between the three MXenes, we calculate the specific heat, average group velocity, and average electron relaxation time, as listed in Table I. The corresponding values for Cu are also listed for comparison. Note that the average electron group velocity and average relaxation time are determined using the weighted average [53], and the expressions are provided in the Supplemental Material [25]. As shown in Table I, the smaller electronic thermal conductivity of MXenes compared to Cu is due to the smaller average electron group velocity and average relaxation time. On the other hand, although the three MXenes have a similar geometry, the electronic thermal conductivity of Ti<sub>2</sub>C(OH)<sub>2</sub> is only about half of the others. This can be attributed to the small average electron group velocity and average relaxation time in Ti<sub>2</sub>C(OH)<sub>2</sub>. Even though the thermal conductivities of Ti<sub>2</sub>CCl<sub>2</sub> and Ti<sub>2</sub>CF<sub>2</sub> are similar, the mechanism is different. Ti<sub>2</sub>CCl<sub>2</sub> has a larger average electron relaxation time but a smaller electronic volumetric specific heat compared to Ti<sub>2</sub>CF<sub>2</sub>. The larger average electron relaxation time in Ti<sub>2</sub>CCl<sub>2</sub> is related to its smaller electron-phonon coupling strength, which will be discussed later. The smaller volumetric electronic specific heat of Ti<sub>2</sub>CCl<sub>2</sub> is caused by its larger unit cell volume and smaller electronic density of states (DOS) in the vicinity of the Fermi level among the three MXenes (see Fig. S4). It is worth noting that the average relaxation times (from 8.14 to 16.4 fs in Table I) clearly deviate from the empirical value of 10 fs [54,55].

We further calculate the electrical conductivity of MXenes, as shown in Fig. 3(a). The magnitude of the electrical

conductivity is on the order of  $10^6$  S/m, which is significantly smaller than that of common metals such as Al and Cu [18,56,57]. Our predicted electrical conductivity is larger than the existing experimental data for metallic MXene thin film Ti<sub>3</sub>C<sub>2</sub>T<sub>z</sub> with mixed functional groups ( $6.5 \times 10^5$  S/m) [58]. This difference may be related to the quality of the experimental samples, such as the defects caused by impurities and dislocations. Note that the electrical conductivity of Ti<sub>2</sub>CF<sub>2</sub> and Ti<sub>2</sub>CCl<sub>2</sub> are very close, while Ti<sub>2</sub>C(OH)<sub>2</sub> has the smallest value. We also calculate the Lorenz ratio by  $L = \kappa_{el}/\sigma T$ . As shown in Fig. 3(b), the Lorenz ratio increases with temperature, which is consistent with the Bloch-Grüneisen theory [59]. The calculated Lorenz ratio calculated is smaller than the Sommerfeld value ( $L_0 = 2.44 \times 10^{-8} \text{ W}\Omega/\text{K}^2$ ) at temperatures below 400 K. To understand this phenomenon, we further show the scattering rates of electrons in Fig. 3(c). The scattering rate is not a constant with respect to electron energy. Therefore, the deviation of the Lorenz ratio is ascribed to the energy-dependent electron scattering rates in the vicinity of the Fermi level [18,60]. To further understand the electron scattering process, we decompose the scattering into acoustic and optical phonon scattering. It is found that the electron scattering in metallic MXenes is mainly induced by optical phonons, different from common metals [52] in which the acoustic phonon scattering is dominant. This is ascribed to the large phonon density of states of optical phonons in metallic MXenes shown in Fig. S2. It should be noted that electron-electron scattering is another scattering channel in metals. However, it is only important at extremely low and high temperature [61,62], and thus can be neglected in the temperature range we considered here [52]. To verify this statement, we evaluate the electron-electron scattering rates

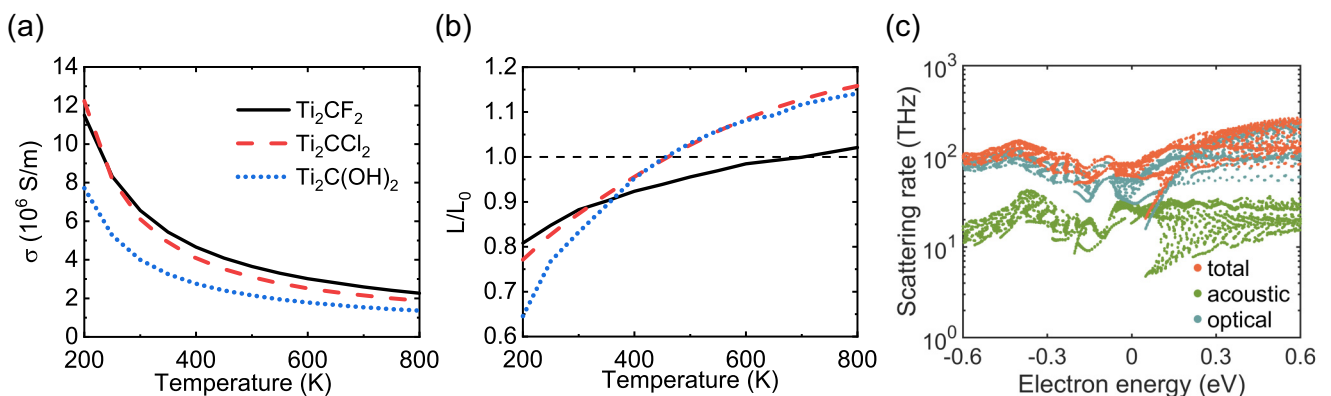


FIG. 3. (a) Electrical conductivity and (b) normalized Lorenz ratio from 200 to 800 K for Ti<sub>2</sub>CF<sub>2</sub>, Ti<sub>2</sub>CCl<sub>2</sub>, and Ti<sub>2</sub>C(OH)<sub>2</sub>. (c) The electron scattering rates from phonons and the resolved scattering rates from acoustic phonons compared to that from optical phonons at 300 K for Ti<sub>2</sub>C(OH)<sub>2</sub>.



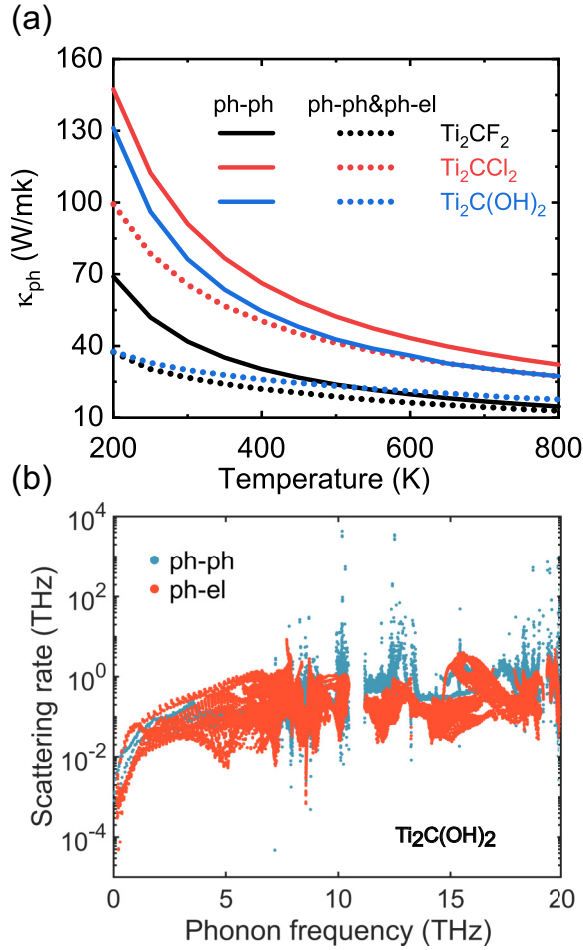


FIG. 4. (a) Phonon thermal conductivity without (solid lines) and with (dashed lines) phonon-electron scattering. (b) The phonon-phonon scattering rates (ph-ph, shown by shallow blue scatters) compared to the phonon-electron scattering rates (ph-el, shown by red scatters) at 300 K for  $Ti_2C(OH)_2$ .

at 300 and 800 K for  $Ti_2C(OH)_2$  with *GW* method in first-principles calculation. It is two orders of magnitude smaller than electron-phonon scattering, as shown in Fig. S6.

#### D. Phonon thermal conductivity

Next, we consider the phonon contribution to thermal conductivity. Note that the phonon thermal conductivity is affected by both the phonon-phonon scattering and phonon-electron scattering. The thermal conductivity considering only phonon-phonon (ph-ph) scattering, and that considering both phonon-phonon and phonon-electron (ph-el) scattering are shown in Fig. 4(a). When only the phonon-phonon scattering is considered, the temperature-dependent phonon thermal conductivity follows the normal  $T^{-1}$  trend. After considering the phonon-electron scattering, the thermal conductivity values for the three MXenes significantly decrease. This is ascribed to the strong electron-phonon coupling, as in metallic carbides [63] and metallic nitrides [64]. Also, the phonon thermal conductivity becomes less temperature dependent when the phonon-electron scattering is included. This is because phonon-electron scattering is not strongly temperature

TABLE II. The phonon thermal conductivity contributed by different phonon branches of the MXenes at 300 K.

Material	ZA (%)	TA (%)	LA (%)	OP (%)
$Ti_2CF_2$	45.1	26.4	20.0	8.5
$Ti_2CCl_2$	39.1	24.9	18.1	17.9
$Ti_2C(OH)_2$	44.5	27.4	14.8	13.3

dependent [63,64]. To show the effect of electron-phonon coupling on the phonon thermal conductivity, we further plot the phonon-electron scattering rates and phonon-phonon scattering rates in Fig. 4(b). The phonon-electron and phonon-phonon scattering rates are comparable, especially for the phonon modes with frequencies below 10 THz. It is also worthy to check the phonon branch contribution to the phonon thermal conductivity. As shown in Table II, although there are many optical phonon (OP) branches for MXenes, the acoustic phonons still dominate the phonon thermal transport. The flexural acoustic phonons contribute the most to the thermal conductivity, while transverse acoustic (TA) and longitudinal acoustic (LA) phonons are also important. The large contribution of the ZA branch is primarily due to the small scattering rates compared to TA and LA phonons (see Fig. S8).

#### E. Analysis of the electron-phonon coupling

The phonon-electron scattering rates can be expressed as [26]

$$\frac{1}{\tau_{\lambda}^{ph-el}} = 2\pi\omega_{\lambda} \sum_{mn} \int_{BZ} \frac{d\mathbf{k}}{\Omega_{BZ}} \left| \delta_{mn}^{\nu}(\mathbf{k}, \mathbf{q}) \right|^2 \times \frac{\partial f_{nk}^0(\mu, T)}{\partial \varepsilon_{nk}} \delta(\varepsilon_{m\mathbf{k}+\mathbf{q}} - \varepsilon_{nk} - \omega_{\lambda}), \quad (2)$$

where  $m$  and  $n$  represent the band indices of electrons,  $\nu$  denotes the phonon polarization,  $\omega$  is the phonon frequency,  $\Omega_{BZ}$  is the volume of the first Brillouin zone.  $\varepsilon$  and  $\mu$  are the electron energy and Fermi level, respectively.  $f^0$  is the equilibrium distribution of the electron.  $g$  is the electron-phonon coupling matrix element. To gain further insights into the strong phonon-electron scattering, we calculate the nesting function [65] and electron-phonon coupling matrix elements [66]. The nesting function is employed to describe the electron-phonon scattering phase space for a specific phonon wave vector, with the expression of [26]

$$\zeta_{\mathbf{q}} = \sum_{mn} \int_{BZ} \frac{d\mathbf{k}}{\Omega_{BZ}} \delta(\varepsilon_{nk} - \mu) \delta(\varepsilon_{m\mathbf{k}+\mathbf{q}} - \mu). \quad (3)$$

Phonons modes with large nesting functions can be severely scattered by electrons. In comparison, the electron-phonon coupling matrix elements reflects the coupling strength between electrons and different phonon modes. Recently, the strong phonon-electron scatterings are ascribed to the large nesting function in several metallic systems, including metallic carbides [63], metallic nitrides [64], and two-dimensional  $Nb_2C$  [67].

We take  $Ti_2C(OH)_2$  as an example. The phonon-electron scattering rates, the nesting function, and electron-phonon

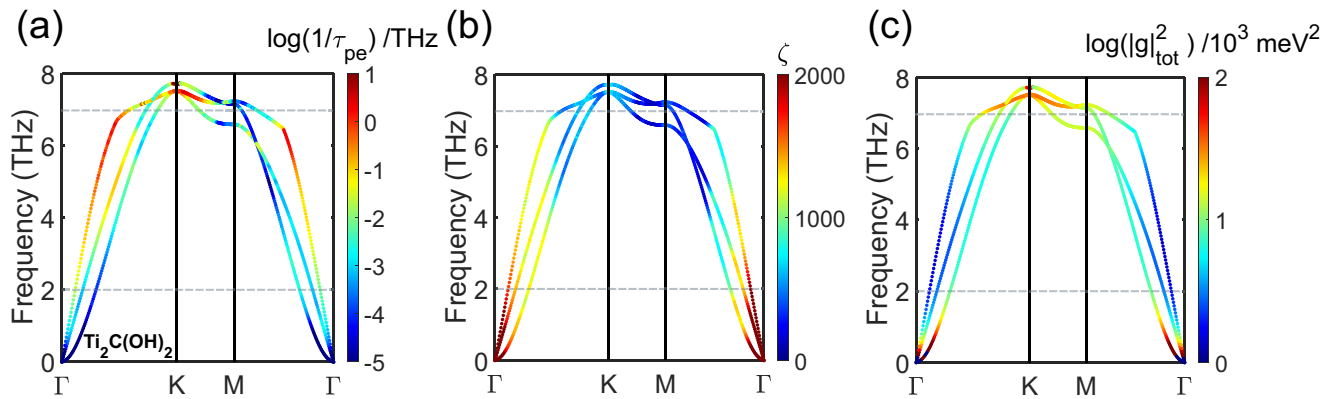


FIG. 5. (a) The phonon-electron scattering rates at 300 K, (b) the nesting function, and (c) the electron-phonon coupling matrix elements mapping onto the three acoustic phonon branches for  $\text{Ti}_2\text{C}(\text{OH})_2$ . Only the electron modes with electron energy 0.2 eV above/below the Fermi level are considered in the calculation of the electron-phonon coupling matrix elements.

coupling matrix elements are mapped onto the phonon dispersion, as shown in Figs. 5(a), 5(b), and 5(c), respectively. Since the acoustic phonons dominate the phonon thermal conductivity, we only present the three acoustic branches here. As the phonon-electron scattering rate is proportional to the phonon frequency, shown in Eq. (2), the contribution from low frequency ( $<2$  THz) is relatively small. In the following, we focus on the frequency range greater than 2 THz. LA branch has the largest phonon-electron scattering rates, while the ZA branch has the lowest value with the same frequency from 2 to 7 THz. This can be reflected by the differences in the nesting function shown in Fig. 5(b). However, for the phonon frequencies larger than 7 THz, the relative magnitudes of phonon-electron scattering rates for different phonon branches cannot be interpreted only by the nesting function. This phenomenon can be elucidated through the electron-phonon coupling matrix elements shown in Fig. 5(c). Therefore, both the nesting function and electron-phonon coupling matrix elements account for the magnitude of phonon-electron scattering rates in metallic MXenes.  $\text{Ti}_2\text{CF}_2$  and  $\text{Ti}_2\text{CCl}_2$  have similar mechanism and the results are shown in Fig. S9.

#### IV. CONCLUSIONS

In summary, we conduct a comprehensive first-principles investigation into the thermal transport properties of 2D metallic MXenes. Both electron and phonon contributions to thermal conductivity are considered. The total thermal conductivities of the MXenes are in the range of 54.3–104.7 W/mK. Electrons are found to have a considerable contribution to the total thermal conductivity, i.e., 37.3–61.3% at 300 K. This is found to be mainly induced by the large electron carrier concentration. Acoustic phonons are the main contributors to the phonon thermal conductivity. Their lifetimes are severely limited by the strong phonon-electron scattering, which is related to both the electron-phonon coupling matrix element and the nesting function.

#### ACKNOWLEDGMENTS

This work was supported by the National Natural Science Foundation of China (NSFC) (Grant No. 52122606). Simulations were performed on the  $\pi$  2.0 cluster supported by the Center for High Performance Computing at Shanghai Jiao Tong University.

- [1] M. Naguib, M. Kurtoglu, V. Presser, J. Lu, J. Niu, M. Heon, L. Hultman, Y. Gogotsi, and M. W. Barsoum, Two-dimensional nanocrystals produced by exfoliation of  $\text{Ti}_3\text{AlC}_2$ , *Adv. Mater.* **23**, 4248 (2011).
- [2] C. Jiang, C. Wu, X. Li, Y. Yao, L. Lan, F. Zhao, Z. Ye, Y. Ying, and J. Ping, All-electrospun flexible triboelectric nanogenerator based on metallic MXene nanosheets, *Nano Energy* **59**, 268 (2019).
- [3] M.-Q. Zhao, M. Torelli, C. E. Ren, M. Ghidui, Z. Ling, B. Anasori, M. W. Barsoum, and Y. Gogotsi, 2D titanium carbide and transition metal oxides hybrid electrodes for Li-ion storage, *Nano Energy* **30**, 603 (2016).
- [4] H.-C. Fu, V. Ramalingam, H. Kim, C.-H. Lin, X. Fang, H. N. Alshareef, and J.-H. He, MXene-contacted silicon solar cells with 11.5% efficiency, *Adv. Energy Mater.* **9**, 1900180 (2019).
- [5] Q. Li, J. Zhou, F. Li, and Z. Sun, Spring-roll-like  $\text{Ti}_3\text{C}_2$  MXene/carbon-coated  $\text{Fe}_3\text{O}_4$  composite as a long-life Li-ion storage material, *Inorg. Chem. Front.* **7**, 3491 (2020).
- [6] J. Li, Q. Peng, J. Zhou, and Z. Sun,  $\text{MoS}_2/\text{Ti}_2\text{CT}_2$  ( $T = \text{F}, \text{O}$ ) heterostructures as promising flexible anodes for lithium/sodium ion batteries, *J. Phys. Chem. C* **123**, 11493 (2019).
- [7] S. J. Kim, H.-J. Koh, C. E. Ren, O. Kwon, K. Maleski, S.-Y. Cho, B. Anasori, C.-K. Kim, Y.-K. Choi, J. Kim, Y. Gogotsi, and H.-T. Jung, Metallic  $\text{Ti}_3\text{C}_2\text{T}_x$  MXene gas sensors with ultrahigh signal-to-noise ratio, *ACS Nano* **12**, 986 (2018).
- [8] Y. Zhang, R. Xiong, B. Sa, J. Zhou, and Z. Sun, MXenes: Promising donor and acceptor materials for high-efficiency heterostructure solar cells, *Sustain. Energ. Fuels* **5**, 135 (2021).
- [9] Q. Li, B. Zhong, W. Zhang, Z. Jia, D. Jia, S. Qin, J. Wang, J. M. Razal, and X. Wang,  $\text{Ti}_3\text{C}_2$  MXene as a new nanofiller

- for robust and conductive elastomer composites, *Nanoscale* **11**, 14712 (2019).
- [10] M. Aakyyir, S. Araby, A. Michelmore, Q. Meng, Y. Amer, Y. Yao, M. Li, X. Wu, L. Zhang, and J. Ma, Elastomer nanocomposites containing MXene for mechanical robustness and electrical and thermal conductivity, *Nanotechnology* **31**, 315715 (2020).
- [11] J. Gu, J. She, and Y. Yue, Micro/nanoscale thermal characterization based on spectroscopy techniques, *ES Energy Environ.* **9**, 15 (2020).
- [12] Z. Fan, L. F. C. Pereira, H.-Q. Wang, J.-C. Zheng, D. Donadio, and A. Harju, Force and heat current formulas for many-body potentials in molecular dynamics simulations with applications to thermal conductivity calculations, *Phys. Rev. B* **92**, 094301 (2015).
- [13] L. Lindsay, D. A. Broido, and N. Mingo, Flexural phonons and thermal transport in graphene, *Phys. Rev. B* **82**, 115427 (2010).
- [14] Z. Gao, F. Tao, and J. Ren, Unusually low thermal conductivity of atomically thin 2D tellurium, *Nanoscale* **10**, 12997 (2018).
- [15] T.-H. Liu, J. Zhou, M. Li, Z. Ding, Q. Song, B. Liao, L. Fu, and G. Chen, Electron mean-free-path filtering in Dirac material for improved thermoelectric performance, *Proc. Natl. Acad. Sci. USA* **115**, 879 (2018).
- [16] Y. Chen, J. Ma, and W. Li, Understanding the thermal conductivity and Lorenz number in tungsten from first principles, *Phys. Rev. B* **99**, 020305 (2019).
- [17] A. Jain and A. J. H. McGaughey, Thermal transport by phonons and electrons in aluminum, silver, and gold from first principles, *Phys. Rev. B* **93**, 081206 (2016).
- [18] S. Li, Z. Tong, X. Zhang, and H. Bao, Thermal conductivity and Lorenz ratio of metals at intermediate temperatures with mode-level first-principles analysis, *Phys. Rev. B* **102**, 174306 (2020).
- [19] T. Wang, Z. Gui, A. Janotti, C. Ni, and P. Karandikar, Strong effect of electron-phonon interaction on the lattice thermal conductivity in 3C-SiC, *Phys. Rev. Mater.* **1**, 034601 (2017).
- [20] D.-S. Tang, G.-Z. Qin, M. Hu, and B.-Y. Cao, Thermal transport properties of GaN with biaxial strain and electron-phonon coupling, *J. Appl. Phys.* **127**, 035102 (2020).
- [21] H. Bao, J. Chen, X. Gu, and B. Cao, A review of simulation methods in micro/nanoscale heat conduction, *ES Energy Environ.* **1**, 16 (2018).
- [22] Z. Tong and H. Bao, Decompose the electron and phonon thermal transport of intermetallic compounds NiAl and Ni<sub>3</sub>Al by first-principles calculations, *Int. J. Heat Mass Transfer* **117**, 972 (2018).
- [23] Z. Guo, N. Miao, J. Zhou, Y. Pan, and Z. Sun, Coincident modulation of lattice and electron thermal transport performance in MXenes via surface functionalization, *Phys. Chem. Chem. Phys.* **20**, 19689 (2018).
- [24] G. Chen, *Nanoscale Energy Transport and Conversion: A Parallel Treatment of Electrons, Molecules, Phonons, and Photons* (Oxford University Press, New York, 2005).
- [25] See Supplemental Material at <http://link.aps.org/supplemental/10.1103/PhysRevMaterials.6.014009> for the expressions for electron and phonon scattering rates and thermal conductivities, computational details, the phonon dispersion with DOS, the electron band structure with DOS, the related results for Ti<sub>2</sub>CF<sub>2</sub> and Ti<sub>2</sub>CCl<sub>2</sub>, and the accumulation functions of phonon and electronic thermal conductivity.
- [26] S. Ponc e, E. R. Margine, C. Verdi, and F. Giustino, EPW: Electron-phonon coupling, transport and superconducting properties using maximally localized Wannier functions, *Comput. Phys. Commun.* **209**, 116 (2016).
- [27] A. A. Mostofi, J. R. Yates, Y.-S. Lee, I. Souza, D. Vanderbilt, and N. Marzari, WANNIER90: A tool for obtaining maximally-localised Wannier functions, *Comput. Phys. Commun.* **178**, 685 (2008).
- [28] V. P. Zhukov, E. V. Chulkov, and P. M. Echenique, GW+T theory of excited electron lifetimes in metals, *Phys. Rev. B* **72**, 155109 (2005).
- [29] A. Marini, C. Hogan, M. Gruning, and D. Varsano, YAMBO: An ab initio tool for excited state calculations, *Comput. Phys. Commun.* **180**, 1392 (2009).
- [30] D. A. Broido, M. Malorny, G. Birner, N. Mingo, and D. A. Stewart, Intrinsic lattice thermal conductivity of semiconductors from first principles, *Appl. Phys. Lett.* **91**, 231922 (2007).
- [31] X. Gu, Z. Fan, and H. Bao, Thermal conductivity prediction by atomistic simulation methods: Recent advances and detailed comparison, *J. Appl. Phys.* **130**, 210902 (2021).
- [32] M. Omini and A. Sparavigna, Beyond the isotropic-model approximation in the theory of thermal conductivity, *Phys. Rev. B* **53**, 9064 (1996).
- [33] W. Li, J. Carrete, N. A. Katcho, and N. Mingo, ShengBTE: A solver of the Boltzmann transport equation for phonons, *Comput. Phys. Commun.* **185**, 1747 (2014).
- [34] J. M. Ziman, *Electrons and Phonons: The Theory of Transport Phenomena in Solids* (Oxford University Press, Oxford, 2001).
- [35] P. Giannozzi, S. Baroni, N. Bonini, M. Calandra, R. Car, C. Cavazzoni, D. Ceresoli, G. L. Chiarotti, M. Cococcioni, I. Dabo, A. Dal Corso, S. de Gironcoli, S. Fabris, G. Fratesi, R. Gebauer, U. Gerstmann, C. Gougousis, A. Kokalj, M. Lazzeri, L. Martin-Samos, N. Marzari, F. Mauri, R. Mazzarello, S. Paolini, A. Pasquarello, L. Paulatto, C. Sbraccia, S. Scandolo, G. Sclauzero, A. P. Seitsonen, A. Smogunov, P. Umari, and R. M. Wentzcovitch, QUANTUM ESPRESSO: A modular and open-source software project for quantum simulations of materials, *J. Phys.: Condens. Matter* **21**, 395502 (2009).
- [36] J. P. Perdew, K. Burke, and M. Ernzerhof, Generalized Gradient Approximation Made Simple, *Phys. Rev. Lett.* **77**, 3865 (1996).
- [37] C. G. Broyden, The convergence of a class of double-rank minimization algorithms 1. General considerations, *IMA J. Appl. Math.* **6**, 76 (1970).
- [38] R. Fletcher, A new approach to variable metric algorithms, *Comput. J.* **13**, 317 (1970).
- [39] D. Goldfarb, A family of variable-metric methods derived by variational means, *Math. Comput.* **24**, 23 (1970).
- [40] D. F. Shanno, Conditioning of quasi-Newton methods for function minimization, *Math. Comput.* **24**, 647 (1970).
- [41] S. Baroni, S. de Gironcoli, A. Dal Corso, and P. Giannozzi, Phonons and related crystal properties from density-functional perturbation theory, *Rev. Mod. Phys.* **73**, 515 (2001).
- [42] Q. Tang, Z. Zhou, and P. Shen, Are MXenes promising anode materials for Li ion batteries? Computational studies on electronic properties and Li storage capability of Ti<sub>3</sub>C<sub>2</sub> and Ti<sub>3</sub>C<sub>2</sub>X (X = F, OH) monolayer, *J. Am. Chem. Soc.* **134**, 16909 (2012).
- [43] Y. Qin, X.-H. Zha, X. Bai, K. Luo, Q. Huang, Y. Wang, and S. Du, Structural, mechanical and electronic properties of

- two-dimensional chlorine-terminated transition metal carbides and nitrides, *J. Phys.: Condens. Matter* **32**, 135302 (2020).
- [44] W. Li, J. Carrete, and N. Mingo, Thermal conductivity and phonon linewidths of monolayer MoS<sub>2</sub> from first principles, *Appl. Phys. Lett.* **103**, 253103 (2013).
- [45] M. Hu, X. Zhang, and D. Poulikakos, Anomalous thermal response of silicene to uniaxial stretching, *Phys. Rev. B* **87**, 195417 (2013).
- [46] A. N. Gandi, H. N. Alshareef, and U. Schwingenschlöggl, Thermoelectric performance of the MXenes M<sub>2</sub>CO<sub>2</sub> (M = Ti, Zr, or Hf), *Chem. Mater.* **28**, 1647 (2016).
- [47] H. Gholivand, S. Fuladi, Z. Hemmat, A. Salehi-Khojin, and F. Khalili-Araghi, Effect of surface termination on the lattice thermal conductivity of monolayer Ti<sub>3</sub>C<sub>2</sub>T<sub>z</sub> MXenes, *J. Appl. Phys.* **126**, 065101 (2019).
- [48] M. Xu, J. Yang, and L. Liu, Temperature-dependent optical and electrical properties of bulk Ti<sub>2</sub>AlC and two-dimensional MXenes from first-principles, *Physica B* **560**, 146 (2019).
- [49] J. Carrete, W. Li, L. Lindsay, D. A. Broido, L. J. Gallego, and N. Mingo, Physically founded phonon dispersions of few-layer materials and the case of borophene, *Mater. Res. Lett.* **4**, 204 (2016).
- [50] Y. Karaaslan, H. Yapicioglu, and C. Sevik, Assessment of Thermal Transport Properties of Group-III Nitrides: A Classical Molecular Dynamics Study with Transferable Tersoff-Type Interatomic Potentials, *Phys. Rev. Appl.* **13**, 034027 (2020).
- [51] R. Liu and W. Li, High-thermal-stability and high-thermal-conductivity Ti<sub>3</sub>C<sub>2</sub>T<sub>x</sub> MXene/Poly(vinyl alcohol) (PVA) composites, *ACS Omega* **3**, 2609 (2018).
- [52] T. M. Tritt, *Thermal Conductivity: Theory, Properties, and Applications* (Kluwer Academic, New York, 2004).
- [53] S. Li, X. Zhang, and H. Bao, Thermal transport by electrons and phonons in PdTe<sub>2</sub>: An ab initio study, *Phys. Chem. Chem. Phys.* **23**, 5956 (2021).
- [54] M. Khazaei, M. Arai, T. Sasaki, M. Estili, and Y. Sakka, Two-dimensional molybdenum carbides: Potential thermoelectric materials of the MXene family, *Phys. Chem. Chem. Phys.* **16**, 7841 (2014).
- [55] S. Sarikurt, D. Çakır, M. Keçeli, and C. Sevik, The influence of surface functionalization on thermal transport and thermoelectric properties of MXene monolayers, *Nanoscale* **10**, 8859 (2018).
- [56] Z. Tong, S. Li, X. Ruan, and H. Bao, Comprehensive first-principles analysis of phonon thermal conductivity and electron-phonon coupling in different metals, *Phys. Rev. B* **100**, 144306 (2019).
- [57] D. Gall, Electron mean free path in elemental metals, *J. Appl. Phys.* **119**, 085101 (2016).
- [58] A. D. Dillon, M. J. Ghidui, A. L. Krick, J. Griggs, S. J. May, Y. Gogotsi, M. W. Barsoum, and A. T. Fafarman, Highly conductive optical quality solution-processed films of 2D titanium carbide, *Adv. Funct. Mater.* **26**, 4162 (2016).
- [59] A. Lavasani, D. Bulmash, and S. Das Sarma, Wiedemann-Franz law and Fermi liquids, *Phys. Rev. B* **99**, 085104 (2019).
- [60] Y. Hu, S. Li, and H. Bao, First-principles based analysis of thermal transport in metallic nanostructures: Size effect and Wiedemann-Franz law, *Phys. Rev. B* **103**, 104301 (2021).
- [61] J. Bass and K. Fischer, *Electrical Resistivity, Kondo and Spin Fluctuation Systems, Spin Glasses and Thermopower* (Springer, Berlin, 1983), Vol. 15.
- [62] L. V. Pourovskii, J. Mravlje, A. Georges, S. I. Simak, and I. A. Abrikosov, Electron–electron scattering and thermal conductivity of  $\epsilon$ -iron at Earth’s core conditions, *New J. Phys.* **19**, 073022 (2017).
- [63] C. Li, N. K. Ravichandran, L. Lindsay, and D. Broido, Fermi Surface Nesting and Phonon Frequency Gap Drive Anomalous Thermal Transport, *Phys. Rev. Lett.* **121**, 175901 (2018).
- [64] S. Li, A. Wang, Y. Hu, X. Gu, Z. Tong, and H. Bao, Anomalous thermal transport in metallic transition-metal nitrides originated from strong electron–phonon interactions, *Mater. Today Phys.* **15**, 100256 (2020).
- [65] J. Noffsinger, F. Giustino, S. G. Louie, and M. L. Cohen, First-principles study of superconductivity and Fermi-surface nesting in ultrahard transition metal carbides, *Phys. Rev. B* **77**, 180507 (2008).
- [66] F. Giustino, Electron-phonon interactions from first principles, *Rev. Mod. Phys.* **89**, 015003 (2017).
- [67] Y. Huang, J. Zhou, G. Wang, and Z. Sun, Abnormally strong electron–phonon scattering induced unprecedented reduction in lattice thermal conductivity of two-dimensional Nb<sub>2</sub>C, *J. Am. Chem. Soc.* **141**, 8503 (2019).